Predicting wind farm wake interaction with RANS: an investigation of the Coriolis force

van der Laan, Paul; Hansen, Kurt Schaldemose; Sørensen, Niels N.; Réthoré, Pierre-Elouan

Published in:
Journal of Physics: Conference Series (Online)

Link to article, DOI:
10.1088/1742-6596/625/1/012026

Publication date:
2015

Document Version
Publisher's PDF, also known as Version of record

Predicting wind farm wake interaction with RANS: an investigation of the Coriolis force

2015 J. Phys.: Conf. Ser. 625 012026

(http://iopscience.iop.org/1742-6596/625/1/012026)

Predicting wind farm wake interaction with RANS: an investigation of the Coriolis force

M. P. van der Laan[1], K. S. Hansen[2], N. N. Sørensen[1], P.-E. Réthoré[1]

[1]Technical University of Denmark, DTU Wind Energy, Risø Campus, DK-4000 Roskilde, Denmark

[2]Technical University of Denmark, DTU Wind Energy, Lyngby Campus, DK-2800 Kgs. Lyngby, Denmark

E-mail: plaa@dtu.dk

Abstract. A Reynolds-averaged Navier-Stokes code is used to simulate the interaction of two neighboring wind farms. The influence of the Coriolis force is investigated by modeling the atmospheric surface/boundary layer with three different methodologies. The results show that the Coriolis force is negligible for a single wind turbine, small for a single wind farm, but important for simulations of wind farm wake interaction.

1. Introduction

A large number of off-shore wind farms are planned to be build in the North Sea with a relatively close wind farm spacing. Nygaard [1] used the simple NO Jensen engineering wake model [2] to show that wind farm wakes can cause annual energy losses to neighboring wind farms. [1]. While wind turbine wake interaction within wind farms have been studied extensively using engineering wake models [3], Computational Fluid Dynamics (CFD) [4, 5, 6, 7] and mesoscale models [8, 9], the mutual interaction between wind farm wakes is a relatively new research area.

In the EERA-DTOC project, power measurements of a Danish wind farm cluster consisting of two off-shore wind farms, Rødsand II and Nysted, are investigated. In this paper, the measurements are compared with a Reynolds-averaged Navier-Stokes (RANS) code using a modified k-ε turbulence model, which is labeled as the k-ε-f_P turbulence model [10]. While the standard k-ε model is unable to predict the near wake deficit, the k-ε-f_P model shows comparable results with measurements and large-eddy simulations (LES). In previous work, the RANS setup including the k-ε-f_P has been successfully tested for single wind turbine wakes [10] and complete wind farms [7]. RANS does not require large computational resources compared with LES, because RANS is steady state and it allows a relative coarse grid (e.g. a cell spacing of 1/8 of the rotor diameter), while LES is transient and a fine grid is necessary to resolve the important turbulent scales. This enables us to use the RANS setup for large domains, e.g. a wind farm cluster covering an area of 100 km^2, which requires a grid size in the order of 100 million cells.

It is common to assume a simple shear flow in wind turbine wake simulations using RANS. In other words, only the atmospheric surface layer (ASL) is modeled, i.e. a logarithmic velocity profile in neutral stratification. However, the scale of the wind farm cluster is so large that the interaction of the Coriolis force with wind farm wakes can become important. In the present

work, the effect of the Coriolis force on wind turbine wake and wind farm wake interaction is investigated by modeling the entire atmospheric boundary layer (ABL). We use a simplified version of the k-ε model of Koblitz et al.[11] to model an ABL, and it is coupled with the k-ε-f_P model. Only neutral stratification is investigated in order to isolate the effect of the Coriolis force from buoyancy forces. The simplified k-ε model of Koblitz et al. is based on two components: a turbulent length scale limiter to limit the boundary layer height, and the addition of the Coriolis force in the momentum equations. The effect of these components are individually tested and compared with the traditional ASL modeling by defining three methodologies:

- Method I: ASL.
- Method II: ABL (turbulent length scale limiter).
- Method III: ABL Coriolis (turbulent length scale limiter and Coriolis force).

The three methodologies are explained in sections 3-5, and they are applied to three test cases, which are presented in section 2. The results are discussed in section 6.

2. Test cases and measurements

Table 1. Summary of cases and corresponding input parameters for numerical computations.

Case	Description	Measurement data	$I_{H,\infty}$ [%]	$U_{H,\infty}$ [m/s]	D [m]	z_H [m]
1	ASL/ABL profiles	-	7	8	-	-
2	Single wake	-	7	8	82.4	69.0
3	Rødsand II &	SCADA data	7	8	92.6	68.5
	Nysted				82.4	69.0

Three test cases are defined in table 1, and they are used to compare the three methodologies from sections 3-5. All test cases are simulated with a turbulence intensity $I_{H,\infty}$ and velocity $U_{H,\infty}$ at hub height z_H of 7% and 8 m/s, respectively. Note that D corresponds to the rotor diameter. In the first test case, the capability of simulating and sustaining ASL and ABL profiles is investigated. Subsequently, the effect of the ASL/ABL modeling is tested for a single wind turbine wake, that is based on the Bonus 2.3 MW/82 wind turbine. The third test case is a Danish wind farm cluster consisting of the Rødsand II wind farm (90 SWT-2.3-93 wind turbines) and the Nysted wind farm (72 Bonus 2.3 MW/82 wind turbines). The layout is shown in figure 1. The wind farm spacing is around 3 km.

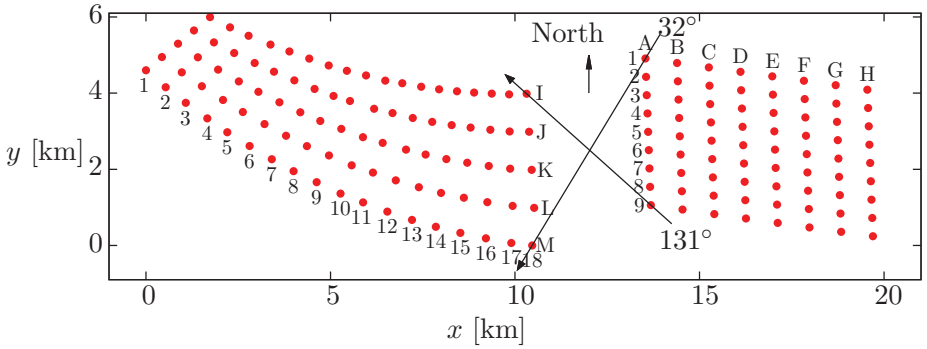

Figure 1. Wind farm layout of the Rødsand II (left) and Nysted (right) wind farms.

Power measurements (SCADA data) of all 162 wind turbines are available; however, the data set of each wind farm cannot be synchronized because the time stamps are not given, which

makes it difficult to determine the free-stream conditions when Rødsand II is operating in the wake of Nysted. This limits the comparison of the measured wind farm interaction with the simulations. In addition, it is not possible to filter the data set from non-neutral atmospheric conditions. We choose to use the measurements for trend comparison only. More information about the measurements can be found in Hansen et al. [12]

3. Method I: ASL

3.1. General setup

EllipSys3D is used as a flow solver, which is originally developed by Sørensen [13] and Michelsen [14]. The RANS equations are solved with a SIMPLE algorithm [15], and a QUICK scheme [16] is used to discretize convective terms. Decoupling of the pressure, velocity and body forces are avoided with a modified Rhie-Chow algorithm [17, 18].

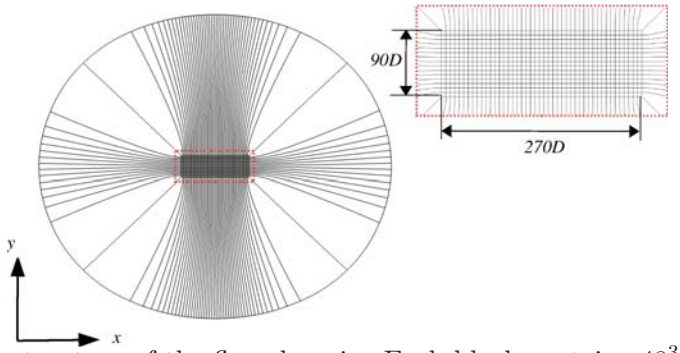

Figure 2. Blocking structure of the flow domain. Each block contains 48^3 cells. Wake domain is shown in red dotted box. Normalization based on $D = 82.4$ m.

The multi-block structure of the flow domain for the wind farm cluster is shown in figure 2, where the dimensions are normalized with $D = 82.4$ m. A region with a uniform spacing of D/8 in all direction is defined, which is labeled as the wake domain. The cell spacing is based on a grid dependency study of single wind turbine simulations [10]. The wake domain has horizontal dimensions of $270\times90\text{D}^2$, large enough to cover both wind farms including a margin of 1 km. The flow and wake domain extend 10D and 3D in the vertical direction, respectively. The wake domain is surrounded by an O-grid with a radius of 50 km. The total grid consist of 795 blocks of 48^3 cells, i.e. 88 million cells. Near the wall, at $z = 0$, the cells are refined in the z-direction, towards a first cell height of 0.5 m. The cells are stretched outside the wake domain. Except for the rough wall at $z = 0$, the flow solver decides if a boundary is an inlet or an outlet, based on the local flow direction. A fully developed flow is assumed at the outlet, while a neutral logarithmic solution is set at the inlet:

$$U(z) = \frac{u_*}{\kappa} \ln\left(\frac{z}{z_0}\right), \qquad k = \frac{u_*^2}{\sqrt{C_\mu}}, \qquad \varepsilon = \frac{u_*^3}{\kappa z}, \tag{1}$$

where U is the stream-wise velocity, u_* is the friction velocity, $\kappa = 0.4$ is the von Kármán constant, z_0 is the roughness height, k is the turbulent kinetic energy, ε is the turbulent dissipation, and C_μ is the eddy-viscosity coefficient. The logarithmic solution is retained through out the domain by setting a rough wall condition at $z = 0$. At the rough wall, the boundary conditions for U and ε are based on an equilibrium of turbulent production and dissipation, while a zero gradient condition is used for the turbulent kinetic energy [19].

The ambient turbulence intensity at hub height $I_{H,\infty}$ is set by the roughness height z_0 in:

$$I_{H,\infty} \equiv \frac{\sqrt{\frac{2}{3}k}}{U_{H,\infty}} = \frac{\kappa\sqrt{\frac{2}{3}}}{\ln\left(\frac{z_H}{z_0}\right)\sqrt[4]{C_\mu}}. \tag{2}$$

Note that C_μ is often used to set $I_{H,\infty}$; however, the behavior of the f_P function in the k-ε-f_P model, as defined in equation (6), changes unphysically with C_μ [20]. The friction velocity u_* is set to obtain the desired hub height velocity. The resulting velocity profile deviates less than 2% in rotor area from a profile that is set with a z_0 based on the site (e.g. 10^{-4} m).

3.2. Wind turbine modeling

The thrust and power curves of the Bonus 2.3 MW/82 and SWT-2.3-93 wind turbines are available, while detailed information about the rotor geometry or wind turbine control is unknown. Therefore, the wind turbines are represented as actuator disks (ADs) [21, 22, 23], that use a simple variable force method [24]. In previous work, it has been shown that the rotational force has a negligible effect on the power deficit [7]. Therefore, it is acceptable to only consider a variable normal force F_N [24]:

$$F_N = \frac{1}{2}\rho C_T^* A\langle U_{AD}^2\rangle, \qquad C_T^* = C_T\frac{U_{H,\infty}^2}{\langle U_{AD}^2\rangle} \tag{3}$$

where $\rho = 1.225$ kg/m^3 is the air density, C_T^* is the thrust coefficient that is based on the disk-averaged velocity $\langle U_{AD}\rangle$, while C_T is the thrust coefficient that is based on the free-stream $U_{H,\infty}$, and A is the rotor area. The normal force is distributed over the AD by multiplying F_N with a normalized force distribution that is obtained from a Detached Eddy Simulation of the NREL-5MW reference wind turbine [23, 25]. During the wind farm simulation, C_T^* is updated per iteration from a C_T^*-$\langle U_{AD}\rangle$ curve, until a satisfactory convergence is reached. The wind turbine power is estimated from a P-$\langle U_{AD}\rangle$ curve. The C_T^*-$\langle U_{AD}\rangle$ and P-$\langle U_{AD}\rangle$ curves are determined from 6 single wind turbine simulations with free-stream velocities between 4 and 9 m/s. In these simulations, a constant thrust force is applied, where F_N is based on a known C_T and a free-stream velocity $U_{H,\infty}$. The procedure is carried out for both wind turbine types.

3.3. Turbulence modeling

The k-ε-f_P turbulence model from van der Laan et al. [10] is applied to the wind farm simulations. The model is based on the standard k-ε model from Launder and Spalding [26]. Both turbulence models can only predict isotropic Reynolds-stresses $\overline{u_i'u_j'}$ because the Boussinesq approximation [27] is used:

$$\overline{u_i'u_j'} = \frac{2}{3}k\delta_{ij} - \nu_T\left(U_{i,j} + U_{j,i}\right), \tag{4}$$

where δ_{ij} is the Kronecker delta, $U_{i,j}$ are the mean velocity gradients and ν_T is the turbulent eddy viscosity:

$$\nu_T = C_\mu f_P\frac{k^2}{\varepsilon}, \tag{5}$$

with C_μ as a constant and ε as the turbulent dissipation. The effective eddy-viscosity coefficient $C_\mu f_P$ is a constant in the standard k-ε model because $f_P = 1$, while f_P is a scalar function in the k-ε-f_P model that depends on the local shear parameter: $\sigma \equiv \frac{k}{\varepsilon}\sqrt{\left(U_{i,j}\right)^2}$. The effective

eddy-viscosity coefficient $C_\mu f_P$ is variable, instead of a constant, which is the only difference with the standard k-ε model. The scalar function f_P in the k-ε-f_P model is defined as [28]:

$$f_P\left(\sigma/\tilde{\sigma}\right) = \frac{2f_0}{1+\sqrt{1+4f_0\left(f_0-1\right)\left(\frac{\sigma}{\tilde{\sigma}}\right)^2}}, \qquad f_0 = \frac{C_R}{C_R-1}, \tag{6}$$

with $\tilde{\sigma} = 1/\sqrt{C_\mu}$ as the shear parameter in an idealized (logarithmic) neutral atmospheric surface layer and C_R is a calibration parameter. In the neutral logarithmic solution, $f_P = 1$ because $\sigma = \tilde{\sigma}$. In regions with a high shear parameter, i.e. $\sigma > \tilde{\sigma}$, $f_P < 1$, and the turbulent eddy viscosity from equation (5) is decreased. The near wind turbine wake is characterized by high velocity gradients, where $\sigma \gg \tilde{\sigma}$. As a result, the k-ε-f_P delays the wake recovery compared to the standard k-ε model. The chosen value of C_R is based on a calibration against LES using eight different single wind turbine cases, as performed in previous work [10].

The standard transport equations for k and ε are used:

$$\frac{Dk}{Dt} = \nabla\cdot\left[\left(\nu+\frac{\nu_T}{\sigma_k}\right)\nabla k\right] + \mathcal{P} - \varepsilon, \qquad \frac{D\varepsilon}{Dt} = \nabla\cdot\left[\left(\nu+\frac{\nu_T}{\sigma_\epsilon}\right)\nabla\varepsilon\right] + \left(C_{\varepsilon,1}\mathcal{P} - C_{\varepsilon,2}\varepsilon\right)\frac{\varepsilon}{k}, \tag{7}$$

where $\mathcal{P}$ is the turbulent production, ν is the kinematic molecular viscosity and $C_{\varepsilon,1}, C_{\varepsilon,2}$, σ_k, σ_ε are constants. The values of the constants are listed in table 2.

The turbulent eddy viscosity from equation (5) can be written as a turbulent velocity scale, i.e. the friction velocity u_*, and a turbulent length scale ℓ_t:

$$\nu_T = C_\mu^{\frac{1}{4}} k^{\frac{1}{2}} C_\mu^{\frac{3}{4}} f_P \frac{k^{\frac{3}{2}}}{\varepsilon} = u_* \ell_t, \quad \Rightarrow \ell_t = C_\mu^{\frac{3}{4}} f_P \frac{k^{\frac{3}{2}}}{\varepsilon}, \tag{8}$$

hence f_P can be seen as a local turbulent length scale limiter, that limits the turbulent length scales in the near wind turbine wake.

Table 2. Model constants.

C_R	C_μ	$C_{\varepsilon,1}$	$C_{\varepsilon,2}$	σ_k	σ_ε	κ
4.5	0.03	1.21	1.92	1.00	1.30	0.40

4. Method II: ABL

4.1. General setup

The wind farm cluster ABL simulations are carried out with the same flow solver and flow domain as discussed in section 3.1. Instead of prescribing the inlet boundaries with the logarithmic solution of equation (1), the inflow is based on a precursor simulation. In the precursor, the flow is driven by a prescribed mass flux, that translates in to a pressure gradient. The flow domain of the precursor simulation is a box that is 6 km high and 1×1 km^2 wide, and it consists of 192×32×32 cells. The lateral boundaries in the inflow direction of the domain are specified as periodic, the bottom boundary is a rough wall as described in section 3.1 and the top and sides are symmetry boundaries where all gradients are set to zero. It is found that a mass flux with a mean velocity of $U = 30.0$ m/s and a roughness of $z_0 = 0.002$ m gives the desired hub height conditions.

4.2. Wind turbine modeling

The wind turbines are modeled in the same way as discussed in section 3.2. It should be noted that the calibration of the thrust coefficient C_T^* is not re-done for the ABL simulations. Hence, it is assumed that the C_T^*-$\langle U_{AD}\rangle$ curve is not affected.

4.3. Turbulence modeling

The turbulence modeling of the ABL simulations is based on the k-ε ABL model of Koblitz et al. [11], where the boundary layer height is finite by limiting the global turbulent length scale ℓ_t:

$$\ell_t = C_\mu^{\frac{3}{4}} \frac{k^{\frac{3}{2}}}{\varepsilon}, \tag{9}$$

using a limiter on ε:

$$\varepsilon = \max\left(C_\mu^{\frac{3}{4}} \frac{k^{\frac{3}{2}}}{l_{t,\max}}, \varepsilon \right), \tag{10}$$

where $l_{t,\max}$ is a chosen maximum turbulent length scale. $l_{t,\max}$ is used to enforce an equilibrium in the transport equation of ε outside the logarithmic region of the ABL, through a height dependent $C_{\varepsilon,1}$, labeled as $C^*_{\varepsilon,1}$, as proposed by Apsley and Castro [29]:

$$C^*_{\varepsilon,1} = C_{\varepsilon,1} + (C_{\varepsilon,2} - C_{\varepsilon,1}) \frac{\ell_t}{l_{t,\max}}. \tag{11}$$

The global turbulent length scale limiter also affects wind turbine wakes similarly to the local turbulent length scale limiter f_P from equation (6). In order to avoid double counting of length scale limitation in the wind farm simulations, the global length scale limiter is switched off in the wake region by multiplying $C^*_{\varepsilon,1}$ with the blending function f_1:

$$f_1 = 0.5 \tanh\left(50\left[f_P - 0.9\right]\right) + 0.5, \tag{12}$$

In addition, equation (10) is not used in the wake domain of the wind farm simulations. The same transport equations for k and ε are used, as defined in equation (7), where the constant $C_{\varepsilon,1}$ is replaced by $f_1 C^*_{\varepsilon,1}$. Ambient values of k and ε are forced by adding the source terms S_k and S_ε to the k and ε equations, respectively, as proposed by Spalart and Rumsey [30]:

$$S_k = \varepsilon_{\text{amb}}, \qquad S_\varepsilon = C_{\varepsilon,2} k^2_{\text{amb}} / \varepsilon_{\text{amb}}, \tag{13}$$

where k_{amb} and ε_{amb} are chosen ambient values: $k_{\text{amb}} = 10^{-4}$ and $\varepsilon_{\text{amb}} = 7.208 \times 10^{-8}$ such that $\ell_t = 1$ above the ABL height.

5. Method III: ABL including Coriolis force

5.1. General setup

The wind farm cluster ABL simulations including the Coriolis force are carried out in the same way as the ABL simulations without Coriolis, as described in section 4; however, the flow is now driven by the Coriolis force and a counter balancing pressure gradient, instead of a prescribed mass flux. A precursor simulation is used to calculate the inflow profiles for the wind farm simulations, as described in section 5. Note that all lateral boundaries are periodic to account for wind veer. It is found that a geostrophic wind of 10.2 m/s and a roughness height of 0.007 m gives the desired conditions at hub height.

The Coriolis force is added to the momentum equation, and it is balanced by a specified constant pressure gradient that is a function of the geostrophic wind G. The resulting volume source $S_{v,i}$ becomes:

$$S_{v,i} = \rho f_c \epsilon_{ijk} \mathrm{e}_k \left(U_j - G_j\right), \tag{14}$$

where ϵ_{ijk} is the Levi-Civita symbol, e_k is the unit vector in the normal direction, G_j is a component of the geostrophic wind G, and f_c is the Coriolis parameter defined as:

$$f_c = 2\omega \sin(\phi), \tag{15}$$

where $\omega = 7.292115 \times 10^{-5}$ rad/s is the rotation of the earth, and ϕ is the latitude. The latitude of the wind cluster is 55.6°, and is assumed to be constant in the simulation, which means that f_c is also a constant. In other words, the global rotation that is induced by the Coriolis force is not modeled. The assumption is valid for the current domain size of 10^2 km, because it is an order smaller than the Rossby radius of 10^3 km. Local flow deflections are still possible, because the Coriolis force is a function of U_j. Hence, wind veer and the interaction of the Coriolis force with wind turbine wakes are modeled. This local flow deflection can be explained using a simple analysis of a flow crossing a roughness change, e.g. a coastal site where the flow moves from sea to land or vice versa. The x and y components of the Coriolis force from equation (14) become:

$$S_{v,x} = \rho f_c \left(V - G_y\right), \quad S_{v,y} = -\rho f_c \left(U - G_x\right), \tag{16}$$

where U and V are the velocity components in x-direction and y-direction, respectively. For simplicity, we consider an incoming flow that is aligned with the x-direction at a certain height, hence $V = 0$ and $S_{v,x}$ is a constant, and only $S_{v,y}$ is responsible for the flow deflection. The local behavior of the Coriolis force is described in table 5.1. Two different flow cases are listed, applicable to the Northern Hemisphere where $f_c > 0$. When the flow moves from sea to land, the flow decelerates and $S_{v,y}$ increases using equation (16), which turns the flow to the left, as also shown by Orr et al. [31]. The opposite occurs when the flow moves from land to sea. The same principle applies to the interaction of the Coriolis force with wind turbines wakes. In regions where the flow is slowed down, the Coriolis force turns the wake to the left, while opposite occurs in regions of wake recovery. The analysis changes if the coastal area or wind farm is located in the Southern Hemisphere, where $f_c < 0$, hence the Coriolis force turns the flow to the right and left for flow deceleration and acceleration, respectively.

Table 3. Local behavior of the Coriolis force in a coastal area in the Northern Hemisphere.

Flow deceleration			Flow acceleration		
sea	$\rightarrow$	land	land	$\rightarrow$	sea
$z_{0,\text{sea}}$	$<$	$z_{0,\text{land}}$	$z_{0,\text{land}}$	$>$	$z_{0,\text{sea}}$
U_{sea}	$>$	U_{land}	U_{land}	$<$	U_{sea}
$S_{v,y,\text{sea}}$	$<$	$S_{v,y,\text{land}}$	$S_{v,y,\text{land}}$	$>$	$S_{v,y,\text{sea}}$
$\rightarrow$ Turning to the left			$\rightarrow$ Turning to the right		

5.2. Wind turbine modeling

The wind turbines are modeled in the same way as discussed in sections 3.2 and 4.2. It should be noted that the wind turbines are not dynamically yawed during the simulations. This means that the local wind direction changes that are caused by the interaction of the Coriolis force and the velocity deficit, can lead to small yaw misalignments. However, similar errors are made in half wake conditions (with or without Coriolis), where a real wind turbine would yaw because the rotor experiences a difference in blade loading, as shown by Schepers et al. [32]

5.3. Turbulence modeling

The global length scale limitation, as discussed in section 4.3, is also necessary in the ABL simulations including Coriolis. Following the k-ε ABL model of Koblitz et al. [11], $l_{\max}$ is estimated from measurements, as described by Blackader [33]:

$$l_{t,\max} = 0.00027\frac{G}{f_c}, \tag{17}$$

where G is the geostrophic wind and f_c is the Coriolis parameter, as defined in equation (15).

6. Results and Discussion

6.1. Test case I: ASL/ABL profiles

The simulated ASL/ABL profiles are shown in figure 3. The dashed lines are ABL results from the precursor simulations or represent the analytical ASL profiles, as defined in equation (1). The solid lines are profiles extracted from empty wind farm domain simulations. All three methods are capable of sustaining the inlet profiles, where only the k-profiles shows some deviation, which is related to the known problem of sustaining k near the wall.

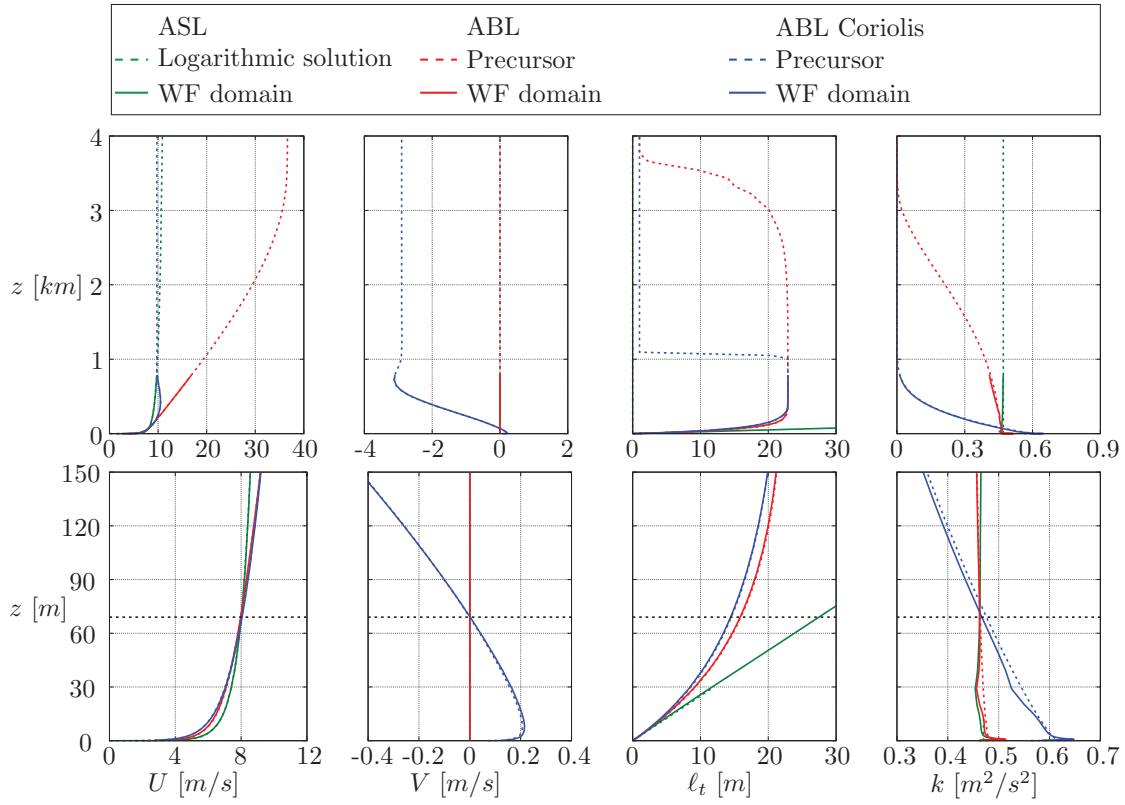

Figure 3. Test case I: Simulated profiles of the precursor and corresponding wind farm (WF) simulations (without wind turbines), extracted at the center of the domain. Bottom plots are a zoomed view of the top plots. Black dotted line represents the hub height (69 m).

As expected, the ABL Coriolis method predicts a wind veer, which is about 0.5 m/s over the rotor area. In addition, the ABL Coriolis method predicts a much lower boundary layer height than ABL method. This is caused by the high mean velocity in the precursor simulation of the ABL method that needs to be set in order to obtain the desired conditions at hub height.

The turbulent length scale ℓ_t predicted by the ASL method grows linearly with z, while the two ABL methods limit ℓ_t. As a results, the ASL-predicted ℓ_t is twice as large at hub height as predicted by the ABL methods.

6.2. Test case II: Single wake

In figure 4, the velocity deficit at hub height of a single wind turbine is plotted at 2D, 7D and 12D downstream. The ABL methods predict similar deficits, while they differ from the ASL method (5% and 3% difference of velocity at the wake center at 7D and 12D, respectively). This is caused by the large difference in the inflow turbulent length scale ℓ_t at hub height, as discussed in section 6.1. A lower ℓ_t reduces the turbulent eddy viscosity, which delays the wake recovery. The wake of the ABL Coriolis method is also slightly skewed because of the Coriolis force, but the impact is negligible.

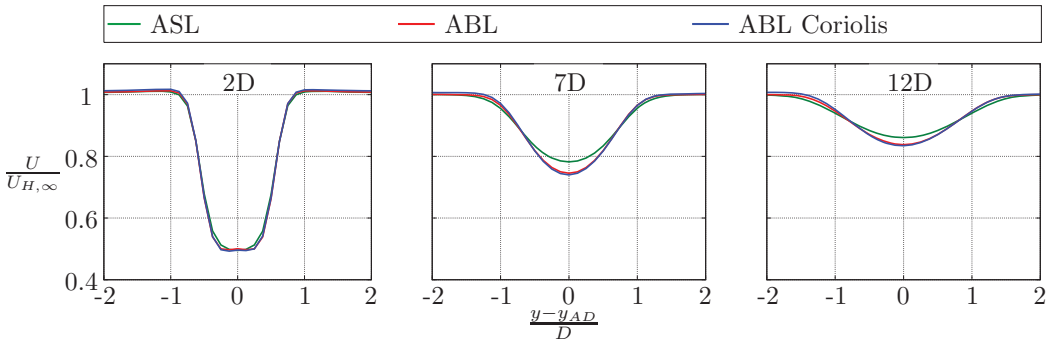

Figure 4. Test case II: Single wake velocity deficit at hub height of the Bonus 2.3 MW/82 wind turbine.

6.3. Test case III: Rødsand II-Nysted

In figure 5, contours of velocity at hub height are plotted in the wind farm cluster simulation. The magnitude of the horizontal velocity components $\sqrt{U^2+V^2}$, and the cross-flow velocity V are shown for a wind direction of 97°. The ABL methods predict larger velocity deficits compared to the ASL method because the free-stream turbulent length scale at hub height is lower, as discussed in section 6.2. The ABL Coriolis method shows similar deficits as the ABL method, although the Coriolis force deflects the wind farm wakes towards the right. This is best visible in the bottom plot of figure 5, where the difference in cross-flow velocity between the ABL Coriolis and the ABL methods is plotted. The difference in cross-flow velocity in the wind farm wake of Nysted is in the order of 0.1 m/s. As a result, the merged wind turbine wakes that originate from rows 1-9 of Nysted move around 0.5D north when they reach the first wind turbines of Rødsand II, 3 km downstream. The lateral movement changes the inflow condition of the wind turbines I18, J18 and K18 (figure 1), from half wake to full wake, as shown in the velocity magnitude plots of the ABL and the ABL Coriolis methods from figure 5. The Coriolis force turns the wind farm wake to the right because the regions of acceleration (wake recovery) are much larger than the regions of deceleration that mainly occur in near vicinity of a wind turbine. Note that the theoretical interaction of the Coriolis force with wind turbines wakes is discussed in section 5.1.

The wind farm efficiency of Rødsand II for a wind direction range of 32-132° is depicted in figure 6. Solid and dashed lines are results with and without Nysted, respectively, while the three colors represent the three different methods from sections 3-5. As expected, all methods predict a lower efficiency of Rødsand II when it is operating in the wake of Nysted. The ASL

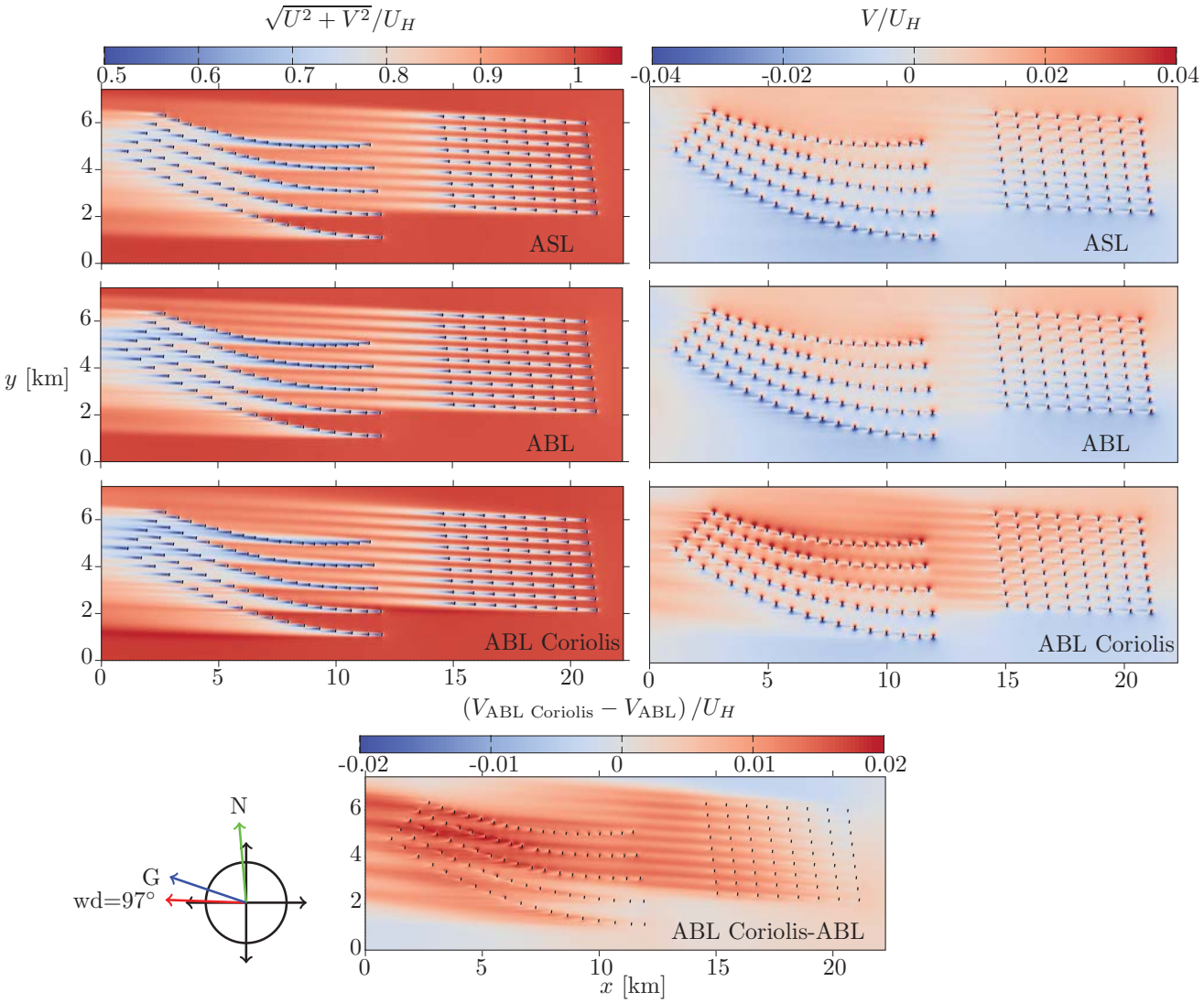

Figure 5. Test case III: Velocity contours in the wind farm cluster. Wind direction is 97° and the north is directed towards a wind direction (wd) of 175°. Left column: magnitude of horizontal velocity, right column: cross-flow velocity, bottom plot: difference in cross-flow velocity between ABL Coriolis and ABL methods.

method predicts a lower impact of Nysted compared to the other the ABL methods, because of the faster wake recovery due to the high free-stream turbulent length scale at hub height in the ASL simulations, as discussed previously. Although not shown in figure 6, it has been found that the influence of Rødsand II to Nysted is small for the Eastern wind sector (0.6% averaged loss in Nysted's wind farm efficiency for wind directions between 32-132°).

The effect of the Coriolis force is best seen when the ABL simulations are compared, such that the effect of the length scale limiter is disregarded. While the Coriolis force has a negligible impact on the single wind turbine simulations (as discussed in section 6.2) and a minor influence on single wind farm simulations (dashed lines), it has a large effect on the wind farm cluster simulations (solid lines). This can be explained as follows. The Coriolis force is a function of the local velocity. When the local velocity is changed by a wind turbine, the local Coriolis force also changes. In the Northern Hemisphere, the Coriolis force increases when the flow decelerates, and the flow is turned to the left, while the opposite occurs for flow acceleration, as discussed

in section 5.1. The effect is not visible for a single wind turbine simulation because the region of modified velocity is too small. In other words, a flow particle does not have enough time to be deflected in such a small space. However, the flow deflection gets stronger when the length scale of the regions with a modified velocity increases, e.g. a wind farm wake. Hence, the flow is most deflected in the wind farm cluster simulations, which in this case increases the alignment of the flow with the arcs in the Rødsand II wind farm. Therefore, the orientation of the curved rows in Rødsand II is unfavorable.

Figure 6 also indicates that Rødsand II loses in order of 10-15% in wind farm efficiency for wind directions between 70-100° because of the presence of Nysted. This eastern wind sector has a probability of 10%, which results into an overall loss of 1-2% for a wind speed of 8 m/s.

The measurements in figure 6 show a similar trend in wind farm efficiency as seen in the wind farm cluster simulations, except for the 107° data point, which is not understood. Unfortunately, the lack of free-stream measurements makes it difficult to make stronger statements.

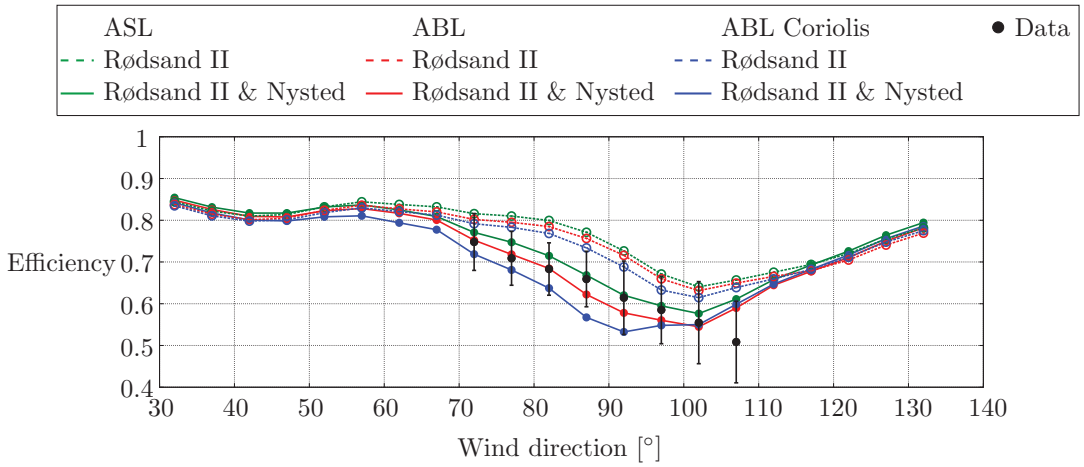

Figure 6. Test case III: Wind farm efficiency of Rødsand II. Solid and dashed lines: with and without Nysted, respectively. Limited data shown for trend comparison only.

7. Conclusions

The effect of the Coriolis force on wind farm wake interaction is investigated in RANS. Three different methodologies of modeling the atmospheric surface/boundary layer are used: ASL method (only modeling the neutral logarithmic region), ABL method (modeling the neutral ABL with a turbulent length scale limiter to limit the boundary height) and the ABL Coriolis method (modeling the neutral ABL with a turbulent length scale limiter including Coriolis forces). All methods can sustain their corresponding inflow profiles in a large wind farm cluster domain. The ABL methods predict a turbulent length scale at hub height that is half of the one simulated by the ASL method, which delays the wake recovery. Therefore, the effect of the Coriolis can only be investigated by comparing the ABL method and the ABL Coriolis method. While the Coriolis force has a negligible impact on a single wind turbine wake and a small effect on a single wind farm, it has a large influence on the wind farm cluster simulation, where the Rødsand II wind farm is operating in the wake of the Nysted wind farm. The Coriolis force deflects the recovering wind farm wake towards the right, which increases the alignment of the Nysted wakes with the curved rows in the Rødsand II wind farm. Therefore, the orientation of the curved rows is predicted to be unfavorable with respect to the sign of the Coriolis force that is present in the Northern Hemisphere. Since the effect of the Coriolis force is significant in a

RANS simulation of a wind farm cluster, it is recommended to include it when wind farm wake interaction is studied.

Acknowledgments
This work is supported by the Center for Computational Wind Turbine Aerodynamics and Atmospheric Turbulence funded by the Danish Council for Strategic Research, grant number: 09-067216, and the EERA-DTOC project funded by FP7-ENERGY-2011-1, grant number: 282797. Computational resources were provided by DCSC and the DTU central computing facility.

References

[1] Nygaard N G 2014 *J. Phys.: Conf. Series* **524** 1
[2] Jensen N O 1983 A note on wind generator interaction Tech. Rep. Risø-M-2411 Risø National Laboratory Roskilde, Denmark
[3] Gaumond M, Réthoré P E, Ott S, Peña A, Bechmann A and Hansen K S 2013 *Wind Energy* **17** 1169
[4] Churchfield M J, Lee S, Moriarty P J, Martinez L A, Leonardi S, Vijayakumar G and Brasseur J G 2012 *AIAA Conference, Nashville, USA* p 1
[5] Port´e-Agel F, Wu Y T and Chen C H 2013 *Energies* **6** 5297
[6] Nilsson K, Ivanell S, Hansen K S, Mikkelsen R, Sørensen J N, Breton S P and Henningson D 2014 *Wind Energy* Published online: DOI: 10.1002/we.1707
[7] van der Laan M P, Sørensen N N, Réthoré P E, Mann J, Kelly M C, Troldborg N, Hansen K S and Murcia J P 2014 *Wind Energy* Published online: DOI: 10.1002/we.1804
[8] Fitch A C, Olson J B, Lundquist J K, Dudhia J, Gupta A K, Michalakes J and Barstad I 2012 *Mon. Wea. Rev.* **140** 3017
[9] Volker P J H, Badger J, Hahmann A N and S O 2015 *Geosci. Model Dev. Discuss.* **8** 3481
[10] van der Laan M P, Sørensen N N, Réthoré P E, Mann J, Kelly M C, Troldborg N, Schepers J G and Machefaux E 2015 *Wind Energy* **18** 889
[11] Koblitz T, Bechmann A, Sogachev A, Sørensen N and Réthoré P E 2015 *Wind Energy* **18** 75
[12] Hansen K S, Réthoré P E, Palma J, Hevia B, Prospathopoulos J, Penã A, Ott S, Schepers G, Palomares A, van der Laan M P and Volker P 2015 *Submitted to J. Phys.: Conf. Series*
[13] Sørensen N N 1994 Ph.D. thesis Risø National Laboratory Roskilde, Denmark
[14] Michelsen J A 1992 Basis3d - a platform for development of multiblock PDE solvers. Tech. Rep. AFM 92-05 Technical University of Denmark, Lyngby, Denmark
[15] Patankar S V and Spalding D B 1972 *Int. J. Heat. Mass. Trans.* **15** 1787
[16] Leonard B P 1979 *Comput. Methods in Appl. Mech. Eng.* **19** 59
[17] Réthoré P E and Sørensen N N 2012 *Wind Energy* **15** 915
[18] Rhie C M and Chow W L 1983 *AIAA Journal* **21** 1525
[19] Sørensen N N, Bechmann A, Johansen J, Myllerup L, Botha P, Vinther S and Nielsen B S 2007 *J. Phys.: Conf. Series* **75** 1
[20] van der Laan M P, Sørensen N N, Réthoré P E, Mann J, Kelly M C and Schepers J G 2013 *Proc. ICOWES2013, Copenhagen, Denmark* p 514
[21] Mikkelsen R 2003 Ph.D. thesis Technical University of Denmark, Mek dept Lyngby, Denmark
[22] Réthoré P E 2009 Ph.D. thesis Aalborg University, Risø DTU Roskilde, Denmark
[23] Réthoré P E, van der Laan M P, Troldborg N, Zahle F and Sørensen N N 2014 *Wind Energy* **17** 919
[24] van der Laan M P, Sørensen N N, Réthoré P E, Mann J, Kelly M C and Troldborg N 2014 *Wind Energy* Published online: DOI: 10.1002/we.1816
[25] Jonkman J, Butterfield S, Musial W and Scott G 2009 Definition of a 5-MW Reference Wind Turbine for Offshore System Development Tech. rep. National Renewable Energy Laboratory
[26] Launder B E and Spalding D B 1972 *Mathematical models of turbulence* (Academic Press, London, UK)
[27] Boussinesq M J 1897 *Théorie de l'écoulement tourbillonnant et tumultueux des liquides* (Gauthier-Villars et fils, Paris, France)
[28] Apsley D D and Leschziner M A 1998 *Int. J. Heat. Fluid. Fl.* **19** 209
[29] Apsley D D and Castro I P 1997 *Bound-Lay. Meteorol.* **83** 75
[30] Spalart P and Rumsey C 2007 *AIAA J.* **45** 2544
[31] Orr A, Hunt J, Capon R, Sommeria J, Cresswell D and Owinoh A 2005 *Weather* 291
[32] Schepers J G, Obdam T S and Prospathopoulos J 2012 *Wind Energy* **15** 575
[33] Blackader A K 1962 *J. Geophys. Res.* **67** 3095